INTERNATIONAL JOURNAL FOR NUMERICAL METHODS IN FLUIDS, VOL. 18, 337–359 (1994)

NUMERICAL SIMULATION OF FREE SHEAR FLOWS AND FAR-FIELD SOUND PRESSURE DIRECTIVITY

W. Y. SOH

Sverdrup Technology, Inc., NASA Lewis Research Center Group, Brook Park, OH 44142, U.S.A.

SUMMARY

An implicit spatial differencing technique with fourth-order accuracy has been developed based on the Pade compact scheme. A dispersion-relation-preserving concept has been incorporated into the numerical scheme. Two-dimensional Euler computation of a spatially developing free shear flow with and without external excitation has been performed to demonstrate the capability of the numerical scheme developed. Results are in good agreement with theory and experimental observation regarding the growth rate of the fluctuating velocity, the convective velocity and the vortex-pairing process. The far-field sound pressure generated by the computed shear flow solution using Lighthill's acoustic analogy shows a strong directivity with a zone of silence at the flow angle.

KEY WORDS Pade compact scheme Dispersion-relation-preserving scheme Free shear flow Large vortical structure Acoustic analogy

INTRODUCTION

Jet noise has emerged as a major issue in the High Speed Civil Transport Program. Noise reduction to an acceptable level set by FAR 36 Stage III is a challenging task to achieve. In order to accomplish this task, it has become increasingly important to be able to predict the sound pressure as a measure of noise level in the aeroacoustic research area. Far-field noise is generated as a byproduct of the jet flow behind the exhaust nozzle. Therefore understanding of this sound source is crucial. Lighthill,[1] through his pioneering acoustic analogy, identified the sound source to be a fluctuating Reynolds stress. Numerous other works, both experimental and analytical, have been focused on the flow turbulence associated with the sound at a distance.

Experimental observations show that the sound power emitted from the jet column is greatest within four or five diameters downstream and then decays rapidly through a transition region. This indicates that the initial development of the jet, before it becomes fully turbulent, should be clearly understood so that an accurate noise prediction can be made. The fully turbulent flow assumption yields analytic results which are far from reality in the developing regions. Freymuth[2] observed organized large-eddy structures in a separated flow of a jet. Brown and Roshko[3] also found a large vortical structure in a free shear layer. The identity of this large vortical structure is discernible even in the fully turbulent region far downstream. Winant and Browand[4] reported that a mechanism of the mixing layer growth is an interaction of adjacent large vortices. These investigators have shown that the flow in free shear layers such as jet and plane mixing flow is well behaved and more organized than previously thought. Shear flow is dominated by large vortical structures which are very predictable and controllable. These flows, which have been thought to be fully turbulent and therefore random and chaotic, have

CCC 0271–2091/94/040337–23

Received 20 January 1993
Revised 7 September 1993

become research subjects with a quite different perspective since the observation of these organized structures. The separation of the organized flow entities from the fully random quantities make it possible to study turbulent shear flows in a certain deterministic way.

A turbulent flow field is made up of a range of length scales from the Kolmogorov scale to the integral scale. If the numerical mesh size can be made fine enough to resolve the smallest scales which dissipate the kinetic energy, then direct numerical simulation (DNS) is the tool to obtain the entire turbulent flow structure. However, the dissipative scale becomes finer as the Reynolds number is increased and the practical hardware limitation is rapidly reached. Therefore the DNS method is limited to simulating only low-Reynolds-number turbulence. For practical computation of higher-Reynolds-number flows, small-scale fluctuations can be modelled so that desired large-scale eddies can be computed directly, while proper dissipation is provided by the small-scale eddy model. This approach, which is referred to as large-eddy simulation (LES), has been successfully employed in many flows with practical applications.

In order to obtain the flow field as the source of sound using DNS or LES, the simulations must be performed using numerical techniques with least distortion and diffusive characteristics. The source of numerical diffusion and phase error is known to be mainly the numerical formulation of convective terms. This numerical artefact gets worse for high-Reynolds-number flow simulations. Typically, free shear flows of interest have very high Reynolds numbers. Therefore a higher-order-accurate numerical scheme which meets the previously mentioned requirements is needed. To develop a highly accurate numerical scheme for this purpose, it will be appropriate to consider only an inviscid flow. A fourth-order Pade implicit differencing scheme with a dispersion-relation-preserving property is introduced in the context of the numerical formulation of the Euler equations. A plane shear flow generated by two streams of air with different velocities is chosen as an example to validate the numerical schemes. Subsonic and supersonic results will be shown and discussed here together with physical observations of the spatial growth of fluctuating velocity, the development of large vortical structure and the vortex-pairing process. Finally, aeroacoustic analysis is made to see the directivity of sound pressure generated by the inviscid shear flow.

GOVERNING EQUATION

The variables T, ρ, $\mathbf{x}$, $\mathbf{u}$, t, p and e represent dimensionless quantities of temperature, density, position, velocity, time, pressure and total energy per mass respectively. The non-dimensionalization is based on reference quantities T_r^*, ρ_r^*, l_r^*, u_r^*, t_r^*, p_r^* and e_r^* with additional definitions $t_r^* = l_r^*/u_r^*$, $p_r^* = \rho_r^* u_r^{*2}$ and $e_r^* = u_r^{*2}$. Then the non-dimensional equation of state can be written as

$$p = \frac{\rho T}{\gamma M_r^2}, \quad \text{with } T = \gamma(\gamma - 1)M_r^2\left(e - \frac{u^2 + v^2}{2}\right),$$

where γ is the ratio of specific heats, $M_r = u_r^*/\sqrt{(\gamma R^* T_r^*)}$ and R^* is the gas constant. The Euler equations in two-dimensional Cartesian co-ordinates (x, y) are

$$\frac{\partial \mathbf{q}}{\partial t} + \frac{\partial \mathbf{f}}{\partial x} + \frac{\partial \mathbf{g}}{\partial y} = 0, \tag{1}$$

where

$$\mathbf{q} = \begin{pmatrix} \rho \\ \rho u \\ \rho v \\ \rho e \end{pmatrix}, \qquad \mathbf{f} = \begin{pmatrix} \rho u \\ \rho u^2 + p \\ \rho uv \\ (\rho e + p)u \end{pmatrix}, \qquad \mathbf{g} = \begin{pmatrix} \rho v \\ \rho uv \\ \rho v^2 + p \\ (\rho e + p)v \end{pmatrix}.$$

The dimensionless speed of sound, c, becomes $\sqrt{T}/M_r$. Equation (1) can be written in generalized co-ordinates (ξ, η) as

$$\frac{\partial \mathbf{Q}}{\partial t} + \frac{\partial \mathbf{F}}{\partial \xi} + \frac{\partial \mathbf{G}}{\partial \eta} = 0, \tag{2}$$

where

$$\mathbf{Q} = J\mathbf{q}, \qquad \mathbf{F} = J(\xi_x \mathbf{f} + \xi_y \mathbf{g}), \qquad \mathbf{G} = J(\eta_x \mathbf{f} + \eta_y \mathbf{g}),$$

with $J = (\xi_x \eta_y - \xi_y \eta_x)^{-1}$.

FORMULATION OF DIFFERENCE SCHEME

Spatial differencing scheme

The Pade compact difference scheme used here is an implicit method in space. The Pade compact scheme[5–7] has also been used previously in flow computations. This scheme uses a symmetric numerical stencil in a compact form so that only a tridiagonal or pentadiagonal matrix inversion is needed. Even for higher-order formulations the compactness is still maintained. The following general form of the Pade difference scheme can be used to obtain a difference form of the first derivative of f:

$$\cdots + \alpha_2 f'_{i-2} + \alpha_1 f'_{i-1} + f'_i + \alpha_1 f'_{i+1} + \alpha_2 f'_{i+2} + \cdots = \cdots + a_2 \frac{f_{i+2} - f_{i-2}}{4h} + a_1 \frac{f_{i+1} - f_{i-1}}{2h},$$

where the subscript i is the mesh index and h is the uniform mesh size. In the present formulation we use the following form to assure that only a tridiagonal matrix inversion is required to obtain a solution for f':

$$\alpha f'_{i-1} + f'_i + \alpha f'_{i+1} = b \frac{f_{i+2} - f_{i-2}}{4h} + a \frac{f_{i+1} - f_{i-1}}{2h}. \tag{3}$$

The above formulation is fourth-order-accurate if $a = (2\alpha + 4)/3$, $b = (4\alpha - 1)/3$ and α is a free parameter. Equation (3) can be sixth-order-accurate if α is set to $\frac{1}{3}$.

To obtain an optimum value of the free parameter α, the dispersion-relation-preserving (DRP) concept is adopted. For an illustration of the DRP method, a fourth-order finite differencing of f' is given explicitly by

$$f' = \tfrac{4}{3} \frac{f_{i+1} - f_{i-1}}{2h} - \tfrac{1}{3} \frac{f_{i+2} - f_{i-2}}{4h}.$$

The above expression is based solely on the truncation of a Taylor series. In unsteady flow computation the order of accuracy is not the only issue to obtain a reliable solution. Unsteady flows by nature contain wave trains, which must be well resolved. Numerical difference formulations constructed solely by truncation of Taylor series do not guarantee wave preserva-

tion even when higher-order differences are used. The wave becomes severely distorted as the wave number or the frequency in a time space is increased and eventually a physical interpretation of the results becomes impossible. Tam and Webb[8] proposed the DRP scheme in which the dispersion characteristics follow closely the original differential form. For example, suppose we construct an explicit difference formulation using six neighbouring points as

$$f' = a\frac{f_{i+1} - f_{i-1}}{2h} + b\frac{f_{i+2} - f_{i-2}}{4h} + c\frac{f_{i+3} - f_{i-3}}{6h}. \tag{4}$$

For this expression to be fourth-order-accurate, the constants b and c must be $(9 - 8a)/5$ and $(3a - 4)/5$ respectively. For $c = 0$ the above expression uses four adjacent points and is based solely on the truncation of a Taylor series. Equation (4) contains the free parameter a which is to be optimized. The central idea of DRP lies in making the discrete form of f' depict the differential form of f' in the Fourier wave space. Thus we define the Fourier transform of $f(x)$ and its inverse as

$$\tilde{f}(\kappa) = \frac{1}{\sqrt{(2\pi)}}\int_{-\infty}^{\infty} f(x)e^{-i\kappa x}\,dx, \qquad f(x) = \frac{1}{\sqrt{(2\pi)}}\int_{-\infty}^{\infty} \tilde{f}(\kappa)e^{i\kappa x}\,d\kappa.$$

Fourier transforming equation (4) using the above definitions gives

$$i\kappa\tilde{f}(\kappa) = \frac{i}{h}\left(a\sin(\kappa h) + \frac{b}{2}\sin(2\kappa h) + \frac{c}{3}\sin(3\kappa h)\right)\tilde{f}(\kappa).$$

Therefore with $\tilde{\kappa} = \kappa h$ we have the wave relation

$$\tilde{\kappa}_n = a\sin(\tilde{\kappa}) + \frac{b}{2}\sin(2\tilde{\kappa}) + \frac{c}{3}\sin(3\tilde{\kappa}). \tag{5}$$

Notice that with the difference approximation given by (4) an input wave number $\tilde{\kappa}$ is distorted numerically into a different wave number $\tilde{\kappa}_n$. It is required to optimize the free parameter a so that the response wave $\tilde{\kappa}_n$ depicts the input wave $\tilde{\kappa}$ closely over the wave number space of interest. In Reference 8 the function to be minimized is chosen as

$$K = \int_{-\pi/2}^{\pi/2} (\tilde{\kappa} - \tilde{\kappa}_n)^2\,d\tilde{\kappa}. \tag{6}$$

The limits of the integral are selected to be $-\pi/2$ and $\pi/2$ under the assumption that a minimum of four mesh intervals are required to resolve a wave. This appears quite plausible, because the value of K becomes very small over a wide range of a for longer waves, e.g. $8h$ or $16h$ waves. For these longer waves optimization based on the DRP concept becomes less meaningful.

Figure 1 shows the numerical behaviour of $\tilde{\kappa}_n/\pi$ against $\tilde{\kappa}/\pi$ for various values of a. The straight line represents the exact differentiation. It is seen that the curve for $a = 1{\cdot}59853$, which has been evaluated to be the optimum in Reference 8, closely follows the straight line for $\tilde{\kappa}/\pi$ up to about 0·5, while the sixth-order counterpart is valid up to about $\tilde{\kappa}/\pi = 0{\cdot}4$. A conventional fourth-order differencing, which is obtained at $a = \frac{4}{3}$, restricts its validity only to a long-wave range, say $\tilde{\kappa}/\pi < 0{\cdot}3$. There is no doubt that the second-order-accurate scheme is severely limited to resolving only long waves.

It is straightforward to make the Pade formulation (3) to be DRP since it has a built-in free

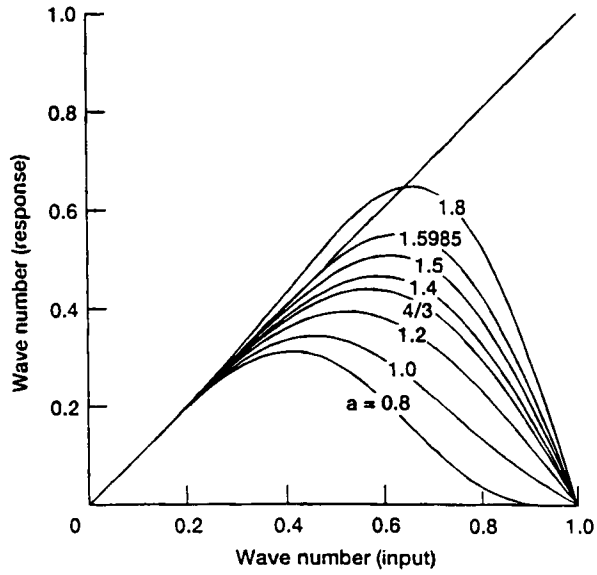

Figure 1. Wave number relation in explicit differencing scheme

parameter α to be optimized. Using the same definition of Fourier transform as used in the explicit example, we can formulate the wave number relation as

$$\tilde{\kappa}_n = \frac{a \sin(\tilde{\kappa}) + (b/2)\sin(2\tilde{\kappa})}{1 + 2\alpha \cos(\tilde{\kappa})}. \tag{7}$$

The optimum value of α is computed to be 0·35619 when the integral K defined by (6) is minimized. Figure 2 illustrates the wave number relation between the input wave $\tilde{\kappa}/\pi$ and the response wave $\tilde{\kappa}_n/\pi$. As was the case with the explicit difference scheme, better wave behaviour is observed for the fourth-order scheme with the optimum α than for the sixth-order differencing with $\alpha = \frac{1}{3}$. The curve for $\alpha = \frac{1}{4}$ is the most compact fourth-order scheme. When comparison is made between the explicit and implicit differencing cases, the most compact fourth-order scheme is seen to have a broader range of wave number than the optimum case of the explicit scheme. A comparison between the Pade scheme and the conventional fourth-order explicit scheme has been given by Soh.[9] Vorticity contour plots of a free shear flow clearly show the supremacy of the Pade compact scheme over the conventional higher-order differencing scheme. However, for a computation which employs a large number of mesh points, such as a three-dimensional flow simulation, the optimized explicit scheme can be a good alternative to implicit differencing if only a moderate number of mesh points have to be added for the resolution of all waves under consideration.

Time-advancing scheme

The four-stage Runge–Kutta technique[10] is adopted for the explicit formulation in time. To obtain new flow variables at $t = (n + 1)\Delta t$ from known data at $t = n\Delta t$, equation (2) is used to advance the solution in time as follows:

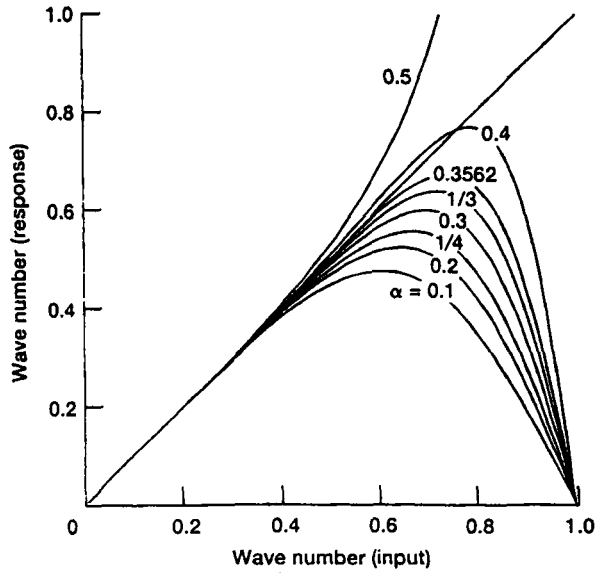

Figure 2. Wave number relation in implicit differencing scheme

$$\mathbf{Q}^{(1)} - \mathbf{Q}^n = \alpha_1 \Delta t \mathbf{W}^{(0)},$$

$$\mathbf{Q}^{(2)} - \mathbf{Q}^n = \alpha_2 \Delta t \mathbf{W}^{(1)},$$

$$\mathbf{Q}^{(3)} - \mathbf{Q}^n = \alpha_3 \Delta t \mathbf{W}^{(2)},$$

$$\mathbf{Q}^{(4)} - \mathbf{Q}^n = \alpha_4 \Delta t \mathbf{W}^{(3)} + \mathbf{D},$$

where $\mathbf{W}^{(k)}$ denotes $\mathbf{S} - \partial\mathbf{F}/\partial\xi - \partial\mathbf{G}/\partial\eta$ evaluated at the kth stage. The stages 0 and 4 are at the times $n\Delta t$ and $(n+1)\Delta t$ respectively. The parameters α_1, α_2, α_3 and α_4 are taken to be $\frac{1}{4}$, $\frac{1}{3}$, $\frac{1}{2}$ and 1 respectively. This time difference is second-order-accurate and the intermediate variables are not stored at every stage.

A numerical dissipation term $\mathbf{D}$ is added during the fourth stage to enhance the numerical stability. The dissipation term is introduced to be of sixth order so that our fourth-order accuracy remains intact:

$$\mathbf{D} = J\omega_e\left(\frac{\partial^6\mathbf{q}}{\partial\xi^6} + \frac{\partial^6\mathbf{q}}{\partial\eta^6}\right),$$

where ω_e is a constant and $\partial^6\mathbf{q}/\partial\xi^6$ is given by

$$\frac{\partial^6\mathbf{q}}{\partial\xi^6} = 15(\mathbf{q}_{i+1,j} + \mathbf{q}_{i-1,j}) - 6(\mathbf{q}_{i+2,j} + \mathbf{q}_{i-2,j}) + (\mathbf{q}_{i+3,j} + \mathbf{q}_{i-3,j}) - 20\mathbf{q}_{ij}.$$

The derivative $\partial^6\mathbf{q}/\partial\eta^6$ in the η-direction is obtained in a similar manner. The value of ω_e is taken to be 0·0125 throughout the free shear flow computations and this artificial dissipation is applied to internal points for $4 \le i \le I-3$ and $4 \le j \le J-3$, where I and J are the maximum grid indices in the ξ- and η-directions respectively. In the present example no numerical instability

arises without the use of artificial damping in the regions of inlet, exit, top and bottom near the boundary. If a numerical instability occurs in the vicinity of the boundary, a biased differenced dissipation term may well be required in the boundary regions.

Boundary conditions

The boundary treatment considered here is a combination of characteristic and algebraic boundary conditions. The characteristic boundary condition solves the governing equation in a characteristic form in each co-ordinate direction and the algebraic boundary condition represents the given boundary conditions such as temperature, total temperature, velocity, *etc.* Equation (2) is written in a non-conservative form as

$$\frac{\partial \mathbf{q}}{\partial t} + \mathbf{A}\frac{\partial \mathbf{q}}{\partial \xi} + \mathbf{B}\frac{\partial \mathbf{q}}{\partial \eta} = 0,$$

where $\mathbf{A} = \partial \mathbf{F}/\partial \mathbf{q}$ and $\mathbf{B} = \partial \mathbf{G}/\partial \mathbf{q}$. For the ξ-direction, equation (2) with the transformation $d\mathbf{q} = \mathbf{R}_\xi\, d\tilde{\mathbf{q}}$ becomes

$$\frac{\partial \tilde{\mathbf{q}}}{\partial t} + \mathbf{R}_\xi^{-1}\mathbf{A}\mathbf{R}_\xi \frac{\partial \tilde{\mathbf{q}}}{\partial \xi} + \mathbf{R}_\xi^{-1}\mathbf{B}\mathbf{R}_\xi \frac{\partial \tilde{\mathbf{q}}}{\partial \eta} = 0.$$

If we construct the matrix $\mathbf{R}_\xi$ such that the eigenvectors of the matrix $\mathbf{A}$ constitute its columns, then the matrix by a similarity transform becomes a diagonal matrix whose entries are the eigenvalues of $\mathbf{A}$ such that

$$\mathbf{R}_\xi^{-1}\mathbf{A}\mathbf{R}_\xi = \mathbf{\Lambda}_\xi = \mathrm{diag}(U,\ U,\ U + a_\xi,\ U - a_\xi),$$

where $a_\xi = c\sqrt{(\xi_x^2 + \xi_y^2)}$. Here c is the speed of sound, defined to be $\sqrt{T}/M_r$, and $U = \xi_x u + \xi_y v$. In the same way, for the η-direction the diagonal matrix becomes

$$\mathbf{R}_\eta^{-1}\mathbf{B}\mathbf{R}_\eta = \mathbf{\Lambda}_\eta = \mathrm{diag}(V,\ V,\ V + a_\eta,\ V - a_\eta),$$

where $a_\eta = c\sqrt{(\eta_x^2 + \eta_y^2)}$ and $V = \eta_x u + \eta_y v$. The characteristic equations are then rewritten in each co-ordinate direction as

$$\mathbf{R}_\xi^{-1}\frac{\partial \mathbf{q}}{\partial t} + \mathbf{\Lambda}_\xi \mathbf{R}_\xi^{-1}\frac{\partial \mathbf{q}}{\partial \xi} + \frac{\mathbf{R}_\xi^{-1}}{J}\frac{\partial \mathbf{G}}{\partial \eta} = 0, \qquad \mathbf{R}_\eta^{-1}\frac{\partial \mathbf{q}}{\partial t} + \mathbf{\Lambda}_\eta \mathbf{R}_\eta^{-1}\frac{\partial \mathbf{q}}{\partial \eta} + \frac{\mathbf{R}_\xi^{-1}}{J}\frac{\partial \mathbf{F}}{\partial \xi} = 0,$$

where

$$\mathbf{R}_\kappa = \begin{pmatrix} 1 & 0 & \dfrac{\rho}{\sqrt{2}c} & \dfrac{\rho}{\sqrt{2}c} \\ u & \rho\tilde{\kappa}_y & \dfrac{\rho}{\sqrt{2}}\left(\dfrac{u}{c} + \tilde{\kappa}_x\right) & \dfrac{\rho}{\sqrt{2}}\left(\dfrac{u}{c} - \tilde{\kappa}_x\right) \\ v & -\rho\tilde{\kappa}_x & \dfrac{\rho}{\sqrt{2}}\left(\dfrac{v}{c} + \tilde{\kappa}_y\right) & \dfrac{\rho}{\sqrt{2}}\left(\dfrac{v}{c} - \tilde{\kappa}_y\right) \\ \dfrac{\Phi}{\gamma - 1} & \rho(u\tilde{\kappa}_y - v\tilde{\kappa}_x) & \Psi + \dfrac{\rho}{\sqrt{2}}\theta & \Psi - \dfrac{\rho}{\sqrt{2}}\theta \end{pmatrix},$$

$$\mathbf{R}_\kappa^{-1} = \begin{pmatrix} 1 - \dfrac{\Phi}{c^2} & (\gamma-1)\dfrac{u}{c^2} & (\gamma-1)\dfrac{v}{c^2} & -\dfrac{\gamma-1}{c^2} \\ \dfrac{-\tilde{\kappa}_y u + \tilde{\kappa}_x v}{\rho} & \dfrac{\tilde{\kappa}_y}{\rho} & \dfrac{-\tilde{\kappa}_x}{\rho} & 0 \\ \dfrac{-\theta}{\sqrt{2}\rho} + \dfrac{\Phi}{\sqrt{2}\rho c} & \dfrac{\tilde{\kappa}_x}{\sqrt{2}\rho} + \dfrac{(1-\gamma)u}{\sqrt{2}\rho c} & \dfrac{\tilde{\kappa}_y}{\sqrt{2}\rho} + \dfrac{(1-\gamma)v}{\sqrt{2}\rho c} & \dfrac{\gamma-1}{\sqrt{2}\rho c} \\ \dfrac{\theta}{\sqrt{2}\rho} + \dfrac{\Phi}{\sqrt{2}\rho c} & \dfrac{-\tilde{\kappa}_x}{\sqrt{2}\rho} + \dfrac{(1-\gamma)u}{\sqrt{2}\rho c} & \dfrac{-\tilde{\kappa}_y}{\sqrt{2}\rho} + \dfrac{(1-\gamma)v}{\sqrt{2}\rho c} & \dfrac{\gamma-1}{\sqrt{2}\rho c} \end{pmatrix},$$

with

$$\tilde{\kappa}_x = \frac{\kappa_x}{\sqrt{(\kappa_x^2 + \kappa_y^2)}}, \qquad \tilde{\kappa}_y = \frac{\kappa_y}{\sqrt{(\kappa_x^2 + \kappa_y^2)}}, \qquad \kappa = \xi, \eta,$$

$$\theta = \tilde{\kappa}_x u + \tilde{\kappa}_y v, \qquad \Phi = \frac{\gamma - 1}{2}(u^2 + v^2), \qquad \Psi = \frac{\rho\Phi}{\sqrt{2}(\gamma-1)c} + \frac{\rho c}{\sqrt{2}(\gamma-1)}.$$

Hedstrom[11] proposed that the non-reflecting boundary condition can be constructed by setting any eigenvalue which is an element of Λ to be zero if a wave is incoming towards the computational domain. Thompson[12] further extended this method and Lele[5] used the same boundary condition in the simulation of a free shear flow. The characteristic boundary condition is not coupled with the Pade formulation but is treated explicitly in space using biased differencing approximation as

$$R_\xi^{-1}\frac{\partial \mathbf{q}_{I,j}}{\partial t} + \tfrac{1}{12}\,\mathrm{diag}(U, U, U + a_\xi, 0)R_\xi^{-1}(25\mathbf{q}_{I,j} - 48\mathbf{q}_{I-1,j} + 36\mathbf{q}_{I-2,j} - 16\mathbf{q}_{I-3,j} + 3\mathbf{q}_{I-4,j}) = 0,$$

$$R_\eta^{-1}\frac{\partial \mathbf{q}_{i,J}}{\partial t} + \tfrac{1}{12}\,\mathrm{diag}(V_t, V_t, V + a_\eta, 0)R_\eta^{-1}(25\mathbf{q}_{i,J} - 48\mathbf{q}_{i,J-1} + 36\mathbf{q}_{i,J-2} - 16\mathbf{q}_{i,J-3} + 3\mathbf{q}_{i,J-4}) = 0,$$

$$R_\eta^{-1}\frac{\partial \mathbf{q}_{i,1}}{\partial t} - \tfrac{1}{12}\,\mathrm{diag}(V_b, V_b, 0, V - a_\eta)R_\eta^{-1}(25\mathbf{q}_{i,1} - 48\mathbf{q}_{i,2} + 36\mathbf{q}_{i,3} - 16\mathbf{q}_{i,4} + 3\mathbf{q}_{i,5}) = 0,$$

where $V_t = \max(V, 0)$ and $V_b = \min(V, 0)$. The above equations are applied to the exit, top and bottom boundaries of a subsonic flow. In the present computation $\partial\mathbf{G}/\partial\eta$ and $\partial\mathbf{F}/\partial\xi$ are omitted in the ξ- and η-directions respectively. At the inlet the characteristic equation is considered only for the wave running at the speed $U - a_\xi$, since the other three conditions are given algebraically. If the flow is supersonic, all the flow variables are provided at the inlet and the zero in the diagonal matrix must be replaced by $\max(U - a_\xi, 0)$ on the exit plane. At a grid point next to the boundary, say $i = I - 1$, the Pade formulation (3) is used in its most compact form by choosing $\alpha = \frac{1}{4}$ as

$$\tfrac{1}{4}f'_{I-2} + f'_{I-1} = -\tfrac{1}{4}f'_I + \tfrac{3}{4}(f_I - f_{I-2})/h.$$

The term f'_I is obtained explicitly by one-sided differencing as used in the characteristic boundary condition.

APPLICATION TO FREE SHEAR FLOW

In the present study Euler computations of plane shear flow are presented to validate the numerical method developed. For this validation, computational results of spatially developing flow are examined against linear theories, experimental data and flow visualizations. The initial shear is given as the axial velocity distribution at $x = 0$, where x is the downstream variable. The initial vorticity thickness of the shear, $\delta\omega_0$, which is defined as $(u_f^* - u_s^*)/(\mathrm{d}u^*/\mathrm{d}y^*)_{max}$, is chosen as the reference length l_r^*. Quantities with asterisks are dimensional and subscripts 'f' and 's' denote faster and slower speeds respectively. The maximum derivative is taken at the inflection point $y = 0$. Then the initial shear profile is given as

$$u = \lambda_s \tanh(2y) + 1, \qquad \lambda_s = \Delta u^*/2u_r^*, \tag{8}$$

where $\Delta u^* = u_f^* - u_s^*$, $u_r^* = (u_f^* + u_s^*)/2$ and the reference velocity in this case is the average speed of the two streams. The momentum thickness θ, which is used as a reference length scale in both theoretical and experimental analyses, becomes $\delta\omega_0/4$ for the shear given by (8). All the flow computations are carried out by assuming that mixing of the two streams occurs at a uniform temperature. The other flow parameters chosen are $T_r^* = 298$ K, $l_r^* = 0{\cdot}00254$ m and $\rho_r^* = 1{\cdot}1839$ kg m^{-3}.

Figure 3 illustrates the two grids used. Grid I (240 × 120) and grid II (300 × 160) are stretched in both the y- and x-directions. In grid I the mesh size Δx varies between 0·4 and 1·568 with $0{\cdot}15 \leqslant \Delta y \leqslant 0{\cdot}4$ at the inlet and $0{\cdot}333 \leqslant \Delta y \leqslant 0{\cdot}864$ at the exit plane. The inlet extends between $-12{\cdot}43 \leqslant y \leqslant 12{\cdot}43$ and the exit plane between $-32{\cdot}7 \leqslant y \leqslant 32{\cdot}7$ and x reaches 196·5. In grid II the mesh size Δx varies between 0·516 and 0·84. The inlet and exit have the same height of $-25{\cdot}8 \leqslant y \leqslant 25{\cdot}8$ with $\Delta y_{min} = 0{\cdot}12$ and $\Delta y_{max} = 0{\cdot}576$. The downstream extends to $x = 206$. The numerical scheme developed has been tested on both grids I and II, but the results presented

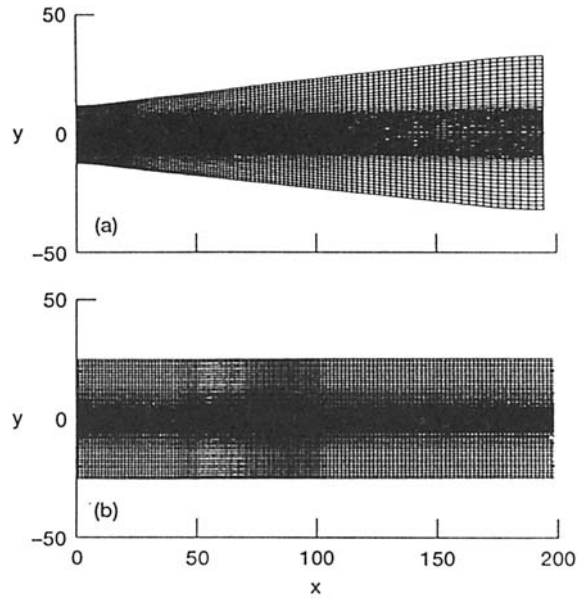

Figure 3. (a) Grid I, 240 × 120. (b) Grid II, 300 × 160

here are obtained on grid II for subsonic flows and on grid I for the supersonic case. The time step is $\Delta t = C_r \Delta y_{min}/(1 + M_r^{-1})$, where C_r takes values between 1·7 and 1·5. It has been observed that a smaller time step size is required for numerical stability when the optimum α is used. When an external forcing is applied, there are 180 and 170 time steps in a forcing time period for the subsonic and supersonic cases respectively.

Subsonic flows are simulated with and without external excitation on the initial shear. The Mach numbers of the two streams considered here are 0·6 and 0·3, with $u_r^* = 155{\cdot}768\ \mathrm{m\,s^{-1}}$, $M_r = 0{\cdot}45$ and $p_r^* = 2{\cdot}873$ kPa. At the inlet u defined by (8), $v = 0$ and $T = 1$ are given and one characteristic equation is solved for the outgoing acoustic wave. At the exit the characteristic equations are solved for the three outgoing waves. For the other incoming acoustic wave the characteristic equation is also imposed with its incoming wave velocity set to zero. On the side boundaries all the characteristic equations are computed by setting the wave velocity to zero if the wave is incoming towards the computational domain. The flow case with no excitation, which is naturally acquired flow, is simulated first. A forcing is then given later on the v-velocity at the inlet from the natural flow solution to excite the flow.

Figures 4(a)–4(c) show the contour plots of vorticity, Mach number and static pressure at an instant in time respectively. A large vortical structure is clearly seen in the Mach number and vorticity contour plots. The static pressure contour plot supports the existence of this

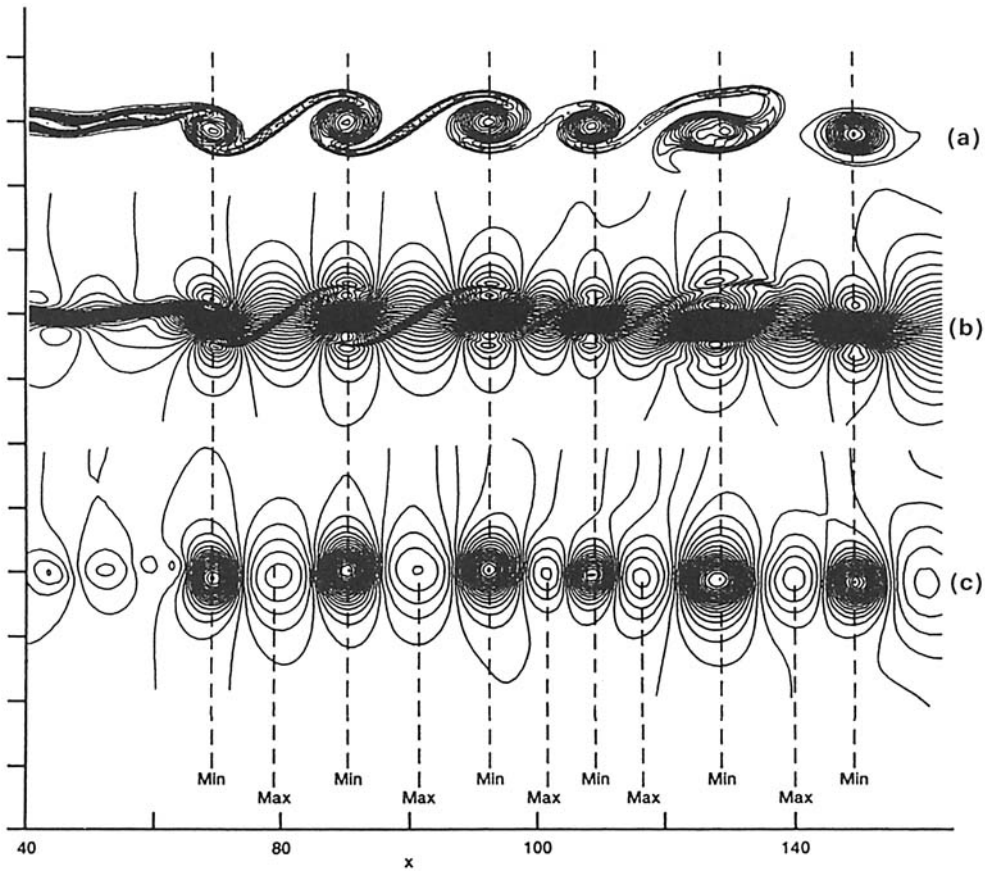

Figure 4. Contours of (a) vorticity, (b) Mach number and (c) static pressure for shear flow with $M = 0{\cdot}6$ and 0·3

vortical structure by aligning its local mimima with the centres of the vortices depicted in the Mach number and vorticity contour plots. This train of local pressure minima and maxima is the basis of analytical estimation of the convective velocity at which the large vortical structure travels. The vorticity contour plot is chosen hereafter as an appropriate visual device to examine the large flow structure. The vorticity contour plots in Figure 5 show a spatial evolution of shear flow with time. The convective velocity can be found from the time history of the vorticity

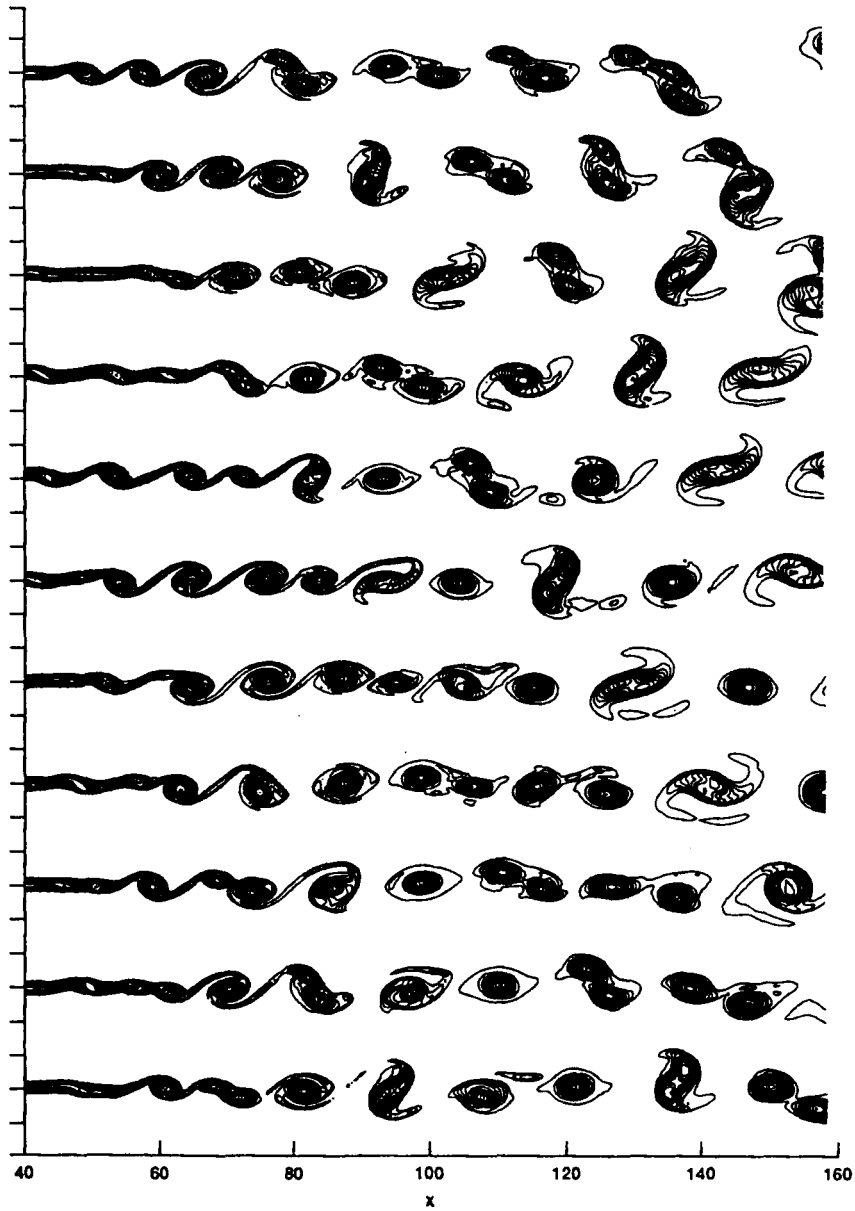

Figure 5. Vorticity contours at every $200\Delta t$ computed by Pade scheme with optimum α

contours. The simulation using Pade differencing with $\alpha = 0{\cdot}3$ and 0·35619 predicts a convective velocity u_c of 0·99. In the explicit computation[9] u_c has a value between 0·96 and 1·02. It can be concluded that the convective velocity is about unity, which is the average velocity of the two streams. Brown and Roshko[3] found that the large eddies travel at a constant velocity, which is the average speed of the two streams, and this velocity is independent of the size and location of the eddy. Papamoschou and Roshko[13] derived the same result. This convective velocity is identical with the computed value and the present results also confirm the earlier observation that the convective velocity is independent of the eddy location and size. The only exception is that the convective velocity varies when two successive vortices merge into one, which is often referred to as vortex pairing. In this pairing process a vortex which travels behind picks up speed to catch up with another vortex proceeding ahead, then the two slide on each other and coalesce. After completion of vortex pairing the convective velocity becomes constant again until another pairing occurs further downstream. This vortex-pairing process is illustrated in the vorticity contour plots. Figure 6 shows the trajectories of vortices, illustrating their birth, pairing, convection and further pairing. Parallel slopes on the $x - t$ diagram, which is the convective velocity, are clearly seen to be constant regardless of the vortex location.

An unforced shear flow exhibits a distributed spectrum in its fluctuating quantity. Figure 7 shows this for the u-velocity spectra at $y = 0$ and various downstream locations. A peak in the spectrum is clearly seen in this unforced flow. The frequency for the peak in the spectrum is referred to as the most preferred frequency. The Strouhal number St is used as a dimensionless frequency and defined to be $f^*\theta/u_1^*$, with f^* the frequency in hertz and θ the initial momentum

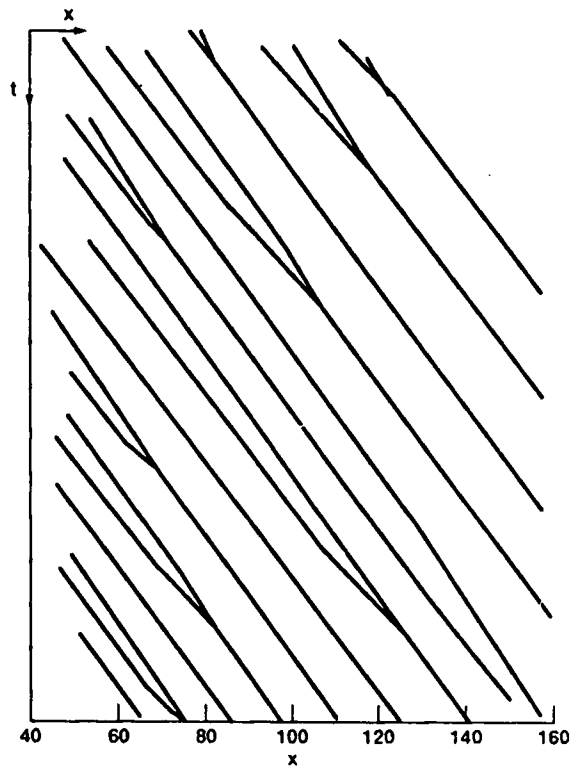

Figure 6. Trajectories of vortices for shear flow with $M = 0{\cdot}6$ and 0·3

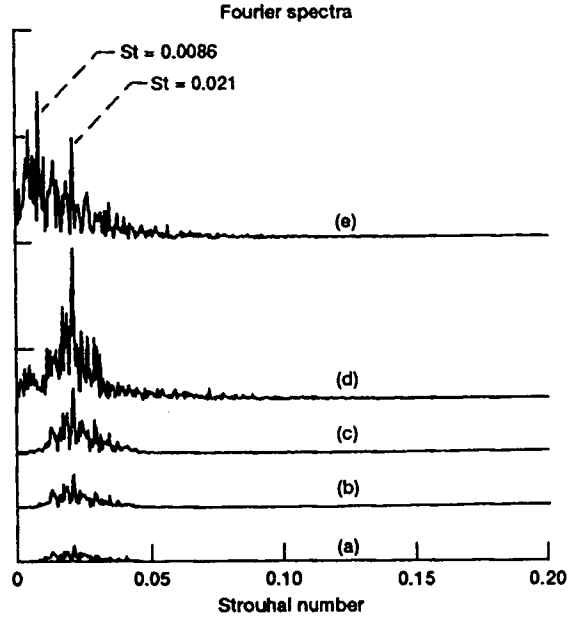

Figure 7. Fourier spectra of u-velocity at $y = 0$: (a) $x = 20{\cdot}65$; (b) $x = 27{\cdot}65$; (c) $x = 34{\cdot}65$; (d) $x = 52{\cdot}84$; (e) $x = 94{\cdot}14$

thickness. In the early flow development the u-spectrum has its peak at $St = 0{\cdot}021$. This persists to some location downstream, then eventually the lower frequency $St = 0{\cdot}0086$ becomes dominant far downstream. This agrees with the general observation that a lower-frequency wave, whose wavelength is longer, survives further downstream than a higher-frequency wave. Linear theories by Michalke[14] and Monkewitz and Huerre[15] show that the most amplified frequency is about $St = 0{\cdot}033$. In jet flow, Freymuth[2] found that the growth rate observed experimentally agrees very well with the theory for St up to about 0·024 and remains constant for $St \geqslant 0{\cdot}024$. This value is very close to the computed St of 0·021. In the light of these results, it appears that the most preferred frequency, which is acquired naturally, has a lower value than the most amplified frequency predicted by linear theory.

It is known from linear theory that a free shear flow is unstable in the presence of a disturbance. The distrubance introduced grows exponentially either in space or in time. The initial shear layer undergoes wave propagation in the presence of a background disturbance, which is due to the truncation error caused by discretization of the flow equations. Travelling instability waves get intensified to a certain level of magnitude. In Figure 5 the shear layer appears wavy, yet it is well connected up to $x = 60$–80 depending upon the time. The shear layer, then, rolls up into a discrete vortex and convects downstream. In the early flow development stage before the vortex roll-up there is a region where linear theory is valid. This linear region can be verified by checking for exponential growth in the magnitude of the fluctuating u-velocity. The RMS fluctuation of u, denoted by u'_{rms}, is used as a measure of the magnitude. Figures 8(a)–8(c) show the region in which the logarithmic scale of u'_{rms} grows linearly for various y-locations. The sharp increase near $x = 0$ should be neglected, since the boundary condition imposed at the inlet influences the flow solution in this region. It appears that the slope also varies with y and the maximum slope is shown on the slower fluid side. The growth rate s is defined as $\mathrm{d}(\ln u'_{\text{rms}})/\mathrm{d}x$.

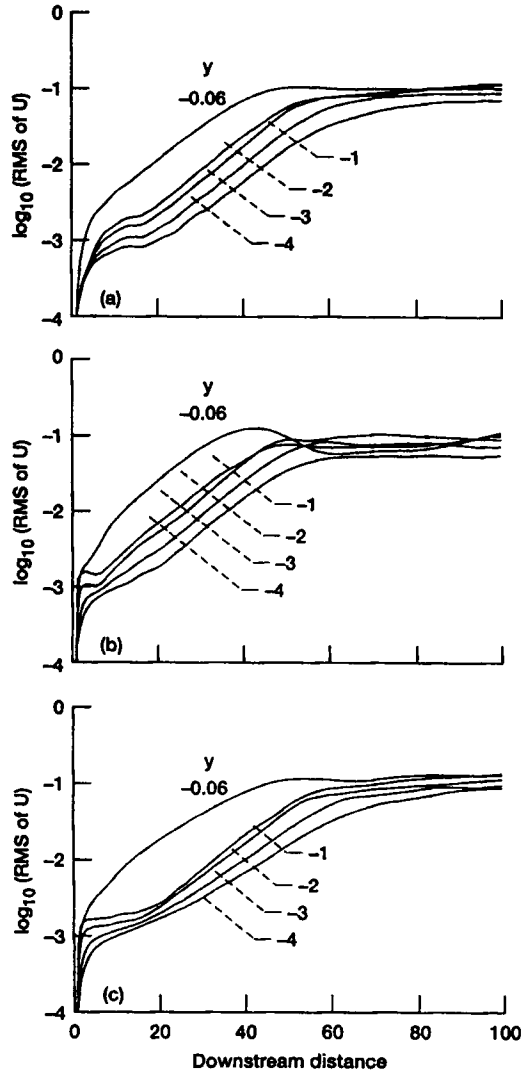

Figure 8. Growth profiles of turbulence intensity u_{rms} along x: (a) unforced; (b) forced with $St = 0{\cdot}021$; (c) forced with $St = 0{\cdot}0086$

Then values of s for the unforced shear flow shown in Figure 8(a) are 0·096, 0·102, 0·106, 0·105, 0·1, 0·099 and 0·096 at $y = -4, -3, -2, -1, -0{\cdot}06$, 1 and 2 respectively. Figure 8(b) presents curves for when forcing is applied at its most preferred upstream frequency $St = 0{\cdot}021$. Values of the slope are the same as those for unforced flow, because the natural shear flow is already dominated by the wave of that frequency. However, the linear region near the inflection point becomes hardly discernible. This can be an indication that non-linearity occurs earlier than in the unforced case. With lower-frequency forcing, s has smaller values of 0·087, 0·096 and 0·098 at $y = -3, -2$ and -1 respectively. It is difficult to find a constant value of s near the inflection point and in the faster fluid territory. This can be interpreted in terms of the two waves, one of

forcing frequency and the other of upstream most preferred frequency, interacting non-linearly. However, it appears in common that u'_{rms} grows to a certain magnitude and then levels off. The u'_{rms} varies in a mildly oscillatory manner further downstream, which is not shown in the figure. In Figures 8(a) and 8(c) u'_{rms} becomes magnified up to about 10% and in Figure 8(b) up to about 13%.

The u'_{rms} discussed above is not for a single frequency but for all the frequency content. To observe the growth behaviour of individual waves, a Fourier decomposition is needed. This has been done for the u-velcoity at $y = 0$ at various downstream distances. The growth rates s computed are 0·065, 0·108 and 0·12 for $St = 0{\cdot}0086$, 0·021 and 0·028 respectively. The exponential growth of the low-frequency wave at $St = 0{\cdot}0086$ is observed at about $65 \leq x \leq 75$, which is sufficiently far downstream that vortex roll-up can occur. Linear wave behaviour is found in the regions $x \leqslant 36$ and $x \leqslant 25$ for $St = 0{\cdot}021$ and 0·028 respectively. The low-frequency expansion given by Monkewitz and Huerre[15] yields values of the growth rate $s(St)$ at $\lambda_s = \frac{1}{3}$ of 0·578, 0·111 and 0·122 in the same order as above.

The profile of u'_{rms} is illustrated in Figure 9. In the early development region kinks appear on both sides of the peak near the centre. The kink on the slower fluid side is very sharp. This phenomenon has been reported in both the experimental literature[2,4,16] and the theoretical literature.[14] Figure 9(a) is for the unforced flow. The u'_{rms} profile first develops into double humps, then evolves into a single peak further downstream. Figure 9(b) also shows the same type of kink in the initial development, but quite a different shape forms downstream. With excitation at the preferred frequency a deep valley appears in the central area. This is similar to the phenomenon Browand[16] found when the shear flow is excited at nearly the most preferred frequency. As flow proceeds further downstream, the profile evolves to a single peak as in the previous case. As shown in Figure 9(c), u'_{rms} under a lower-frequency forcing, which is away from the most preferred upstream frequency, takes on a character similar to the unforced flow. No deep valley is seen in the middle of the flow evolution.

Forcing is introduced to the initial shear to see the more organized flow structure. The transverse velocity v is given an oscillation $\varepsilon g(y) \sin(\omega t)$, where g is a Gaussian distribution. This is similar to the excitation used by Lele.[5] For a subsonic mixing of two streams of $M = 0{\cdot}6$ and 0·3, ε is given as 0·01 and the forcing is applied at the most preferred frequency $St = 0{\cdot}021$. The angular frequency ω is $2\pi/11{\cdot}785$, which equals 5·2 kHz for the flow condition given. Figure 10 shows the vorticity contours at consecutive time periods 192 μs apart. As shown in Figure 5, vortices do not appear to be periodic in the unforced flow, the spacing between two consecutive vortices is irregular and vortex roll-up or merging of two or even three vortices occurs randomly. However, in the presence of forcing, the initial vortex-pairing process is suppressed, with the process resumed at some downstream location. Vortices are orderly, keeping the same distance apart. This is similar to the situation that Ho and Huang[17] observed. As shown in Figure 10, forcing generates a very organized flow structure. This figure also shows that the first five vortices appear frozen, in other words the flow up to about five vortices downstream is stationary. This is the precise counterpart of the flow visualization made in the laboratory using a conditional sampling technique, which can be achieved by synchronizing the strobe speed with the forcing frequency. Vortex pairing occurs downstream, consequently the flow appears to be unsteady in shedding vortices. This vorticity contour also gives the convective velocity as 0·99, which is the same value found for the unexcited case.

A forced superconic free shear flow is also computed with $M = 1{\cdot}6$ and 1·2. The velocity, temperature and density are all given at the inlet. All the characteristic equations are imposed at the exit as boundary conditions. Unlike subsonic flow, it is very difficult (at least in the present computation) to simulate supersonic shear flow without excitation. This indicates that the

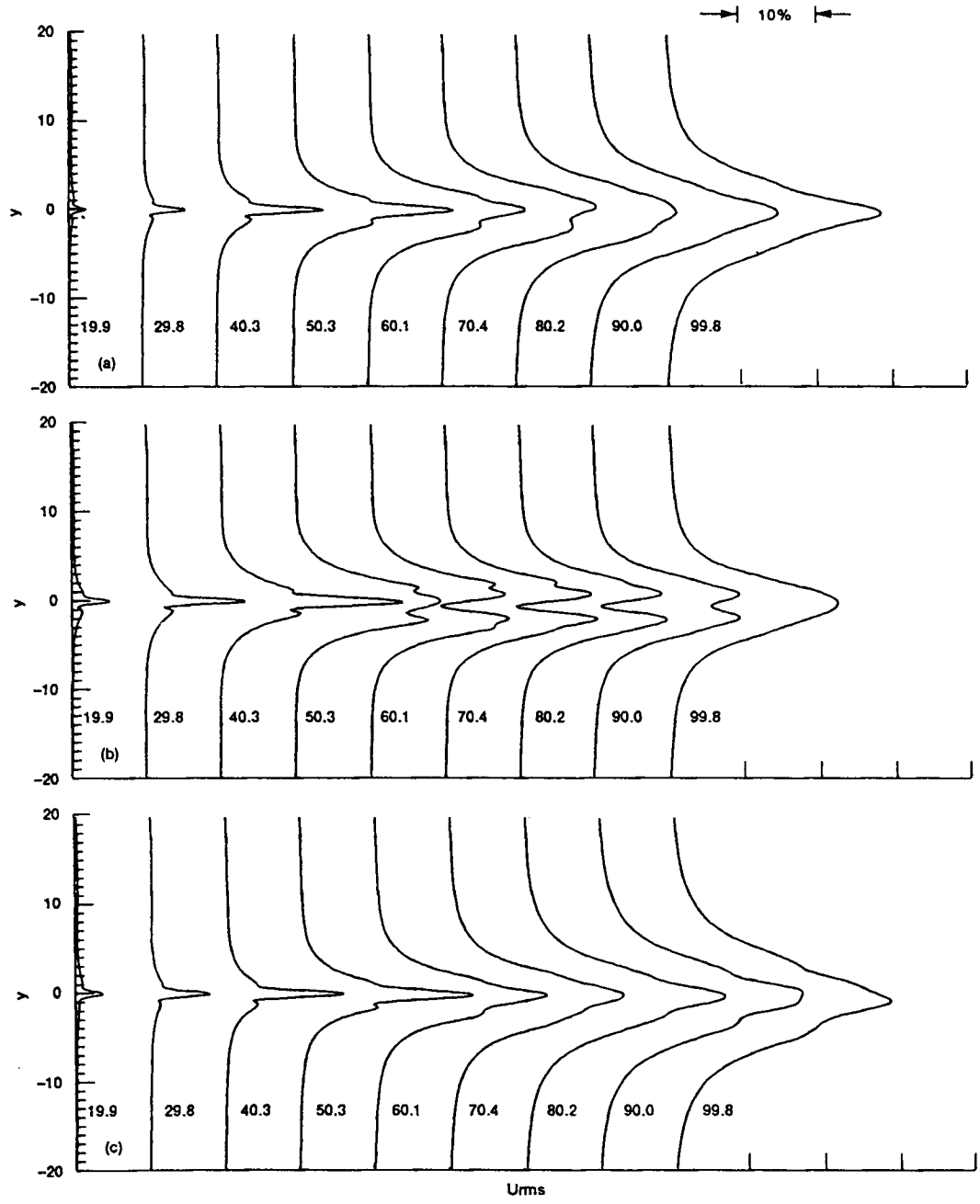

Figure 9. Profiles of u_{rms} along x: (a) unforced; (b) forced at $St = 0{\cdot}021$; (c) forced at $St = 0{\cdot}0086$

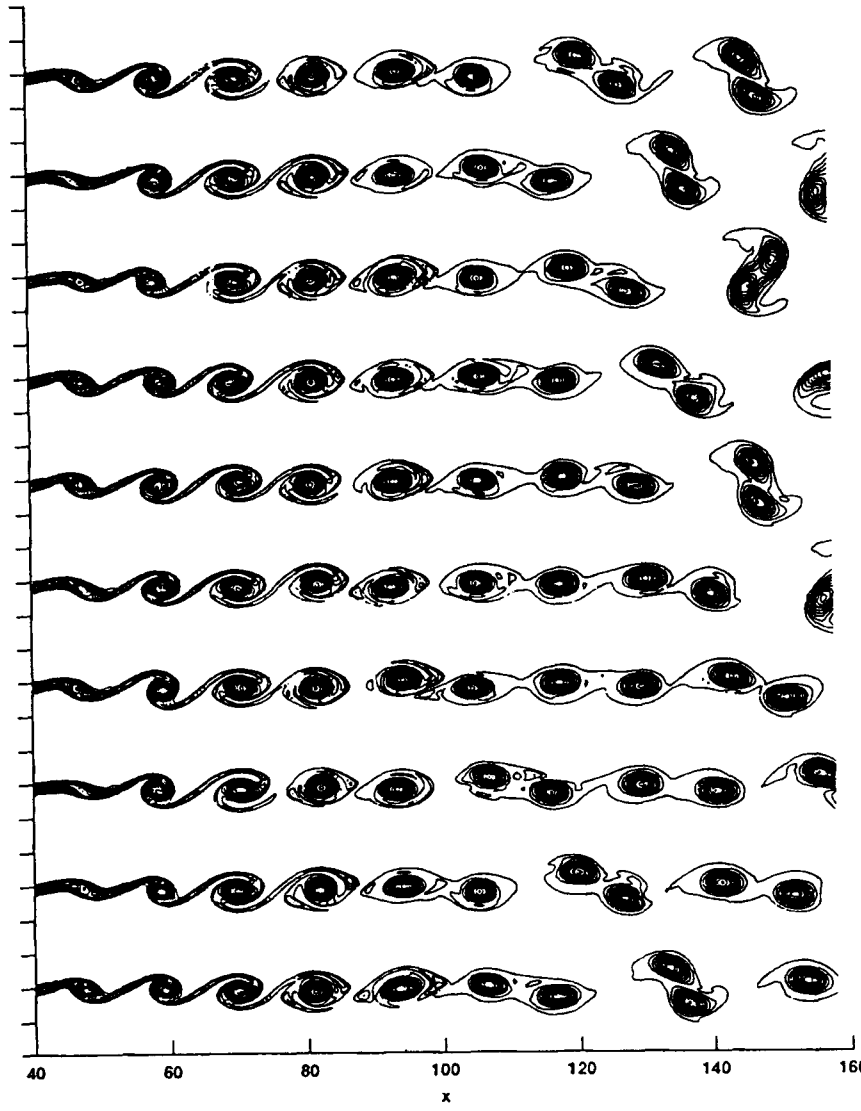

Figure 10. Vorticity contours of forced subsonic flow at every period

nature of the free shear flow generated by two supersonic streams is far more stable than the subsonic flow. An external excitation of $\varepsilon = 0{\cdot}05$ is imposed on the v-velocity at the inlet in a similar manner as used in subsonic flow. The forcing frequency ω is taken arbitrarily to be $2\pi/12{\cdot}29$. Figure 11 shows the flow structure at every two time periods, 128·9 μs apart. It is interesting to observe that no vortex pairing occurs. Many experiments have revealed that the free shear of two supersonic streams exhibits poor mixing characteristics, which is an indication of a very stable flow situation. All the vorticity contour appears identical, because conditional sampling is made on the flow field which is free of vortex-pairing processes. Again, the

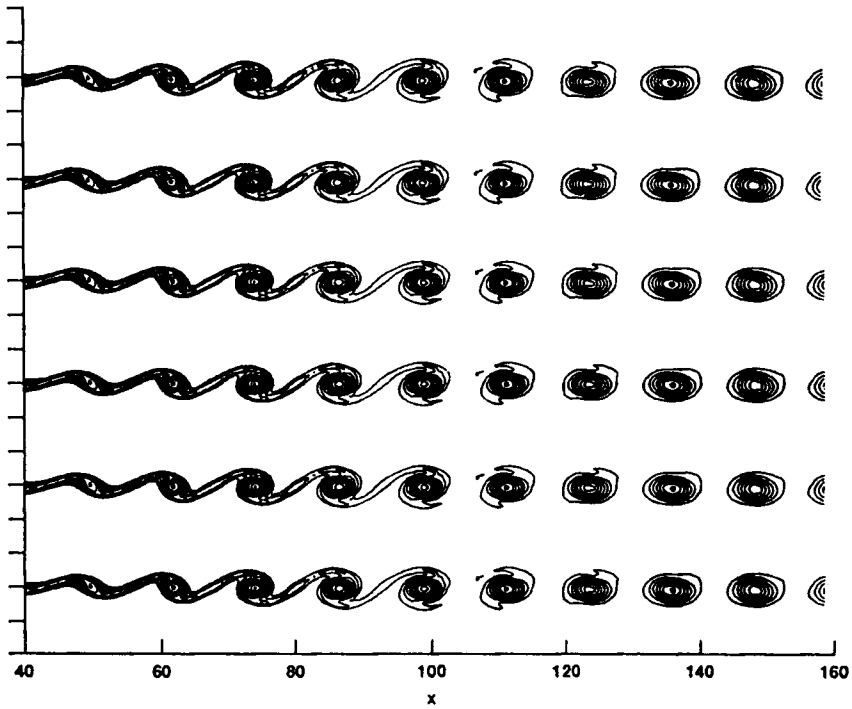

Figure 11. Vorticity contours of forced supersonic flow at every two periods

convective velocity computed from Figure 11 is 0·99. This value is in agreement with Papamoschou and Roshko.[13] From these observations of the excited shear flows it can be concluded that the forcing has no influence on the convective velocity.

DIRECTIVITY OF FAR-FIELD SOUND PRESSURE

According to Lighthill's acoustic analogy,[1] the wave equation for the static pressure p can be obtained by combining the momentum and continuity equations as

$$\frac{\partial^2 p}{\partial t^2} - a_0^2 \frac{\partial^2 p}{\partial x_i^2} = a_0^2 \left(\frac{\partial^2}{\partial x_i \partial x_j} (\rho u_i u_j - \tau_{ij}) - \frac{\partial F_i}{\partial x_i} + \frac{\partial m}{\partial t} \right) + \frac{\partial^2}{\partial t^2} (p - a_0^2 \rho), \tag{9}$$

where a_0 is the reference ambient speed of sound, ρ is the density, τ_{ij} is the viscous stress tensor, F_i is the external force exerted on a unit volume of fluid and m is the mass production per unit volume of fluid. The terms on the right-hand side represent sound sources. With the wave operator on the left-hand side of equation (9), the term $\partial m/\partial t$ without spatial derivative represents the monopole sound source, the first-spatial-derivative term $\partial F_i/\partial x_i$ the dipole source and the second-derivative term the quadrupole source. These monopole and dipole sources play important roles in generating sound from propellers or rotor blades. If we denote the right-hand side of equation (9) by $a_0^2 q(x_i, t)$ and use Fuchs and Michalke's notations,[18] the solution to (9) can be expressed as

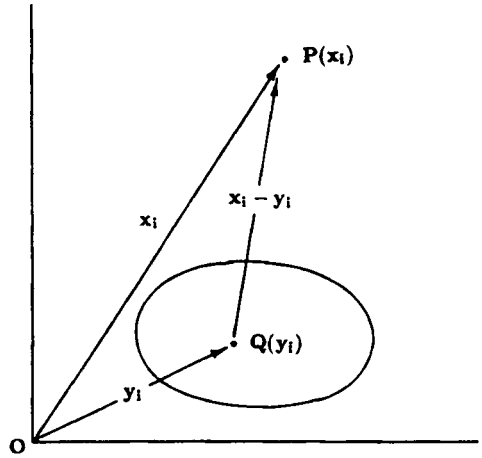

Figure 12. Schematic of far-field and flow field variables

$$p(x_i, t) - p_0 = \frac{1}{4\pi}\int_V \frac{1}{r}[q]^* \, dV(y_i) + \frac{1}{4\pi}\int_A \left(\frac{1}{r}\left[\frac{\partial p}{\partial n}\right]^* + \frac{1}{r^2}\frac{\partial r}{\partial n}[p]^* + \frac{1}{a_0 r}\frac{\partial r}{\partial n}\left[\frac{\partial p}{\partial t}\right]^*\right) dA(y_i). \tag{10}$$

Figure 12 shows the geometric variables used in the above equation. Here $P(x_i)$ is the field point where p is being sought, $Q(y_i)$ is the source point, O is the origin and V and A are the volume and surface respectively of the source over which the volume and surface integrations are to be performed. The quantity $[\cdot]^*$ is defined as

$$[q]^* = q(y_i, t^+) = q(y_i, t - r/a_0), \qquad r = |x_i - y_i|,$$

where t^+ is called the retarded time. In equation (9) the acoustic field is separated from the fluid dynamics under the assumption that the right-hand-side terms are known and no interaction takes place between the sound and fluid flow. If there is no physical obstacle either in motion or stationary, the surface integral in equation (10) vanishes and $\partial m/\partial t$ and $\partial F_i/\partial x_i$ can be dropped out. A low-speed assumption can neglect the pressure deviation from the isentropic state. If it is further assumed that the momentum fluctuation $\rho u_i u_j$ is much larger than the viscous stress, then the sound source due to free shear flow can be approximated only with the quadrupole source and equation (10) can be simplified as

$$p'(x_i) = p(x_i) - p_0 = \frac{1}{4\pi}\int_V \frac{1}{r}\left[\frac{\partial^2 \rho u_i u_j}{\partial y_i \partial y_j}\right]^* dV(y_i). \tag{11}$$

The sound pressure is defined to be the RMS of the pressure. Since the free shear flow computed in the present work is two-dimensional and the fluctuating Reynolds stress $\rho u_i u_j$ never decays with x in the Euler computation (i.e. the sound-producing flow region extends to infinity downstream), it is not practical to obtain the sound pressure level on a realistic decibel scale. However, if we restrict ourselves to the sound pressure contribution only from a certain region of the flow, we can obtain the directivity pattern and compare the sound level between different flow regions. To obtain the directivity contribution, the shear flow regime is divided into fluid

elements, each of which has a unit spanwise length and 10 length units in the flow direction. For the far field, in which r is so large that $r = |x_i - y_i| \approx |x_i|$, the pressure solution (11) becomes the following by substituting the spatial derivative with the time derivative (see details in Reference 18):

$$p'(x_i, t) = \frac{1}{4\pi a_0^2} \frac{x_i x_j}{|x_i|^3} \int_V \left[\frac{\partial^2 \rho u_i u_j}{\partial t^2}\right]^* dV = \frac{\rho}{4\pi a_0^2} \frac{1}{|x_i|} \int_V \left[\frac{\partial^2 \rho u_r^2}{\partial t^2}\right]^* dV, \tag{12}$$

where u_r is the projection of u_i on $\mathbf{r}$ and tensor contraction is employed in the last expression. Under the acoustic far-field assumption on the subsonic flow, the retarded time t^+ distributed over a fluid element can be represented by a single retarded time $t - r/a_0$. The sound pressure p'_{rms}, is computed using equation (12) from each sound-generating fluid element over $10000\Delta t$ and 70 time periods for the unforced and forced cases respectively.

In the polar diagrams in Figures 13 and 14, p'_{rms} is plotted scaled with its local maximum value. The polar diagrams are symmetric with respect to the origin, therefore only the region $-\pi/2 \leqslant \theta \leqslant \pi/2$ is considered in a physical interpretation. The p'_{rms} in Figure 13 is for the unforced flow case. It is clearly seen that the sound pressure pattern by the upstream elements is quite different from that by the downstream elements. The directivity by the fluid element $20 \leqslant x \leqslant 30$ is about $-10°$, which shows that the noise is highest at an angle which is almost aligned with the flow direction if an observer is moving along a circle of large radius with the sound-generating fluid element at the centre. When we take a fluid element downstream, the

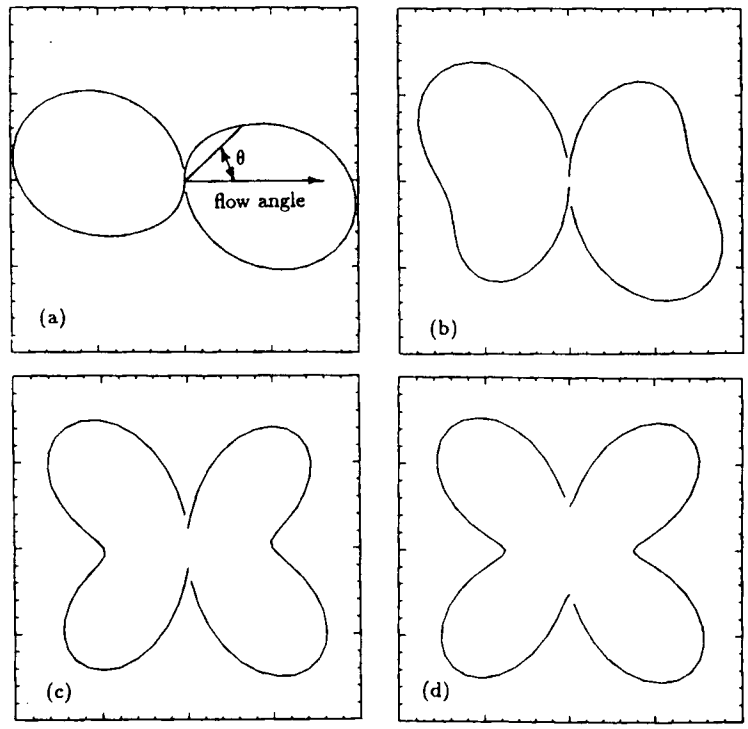

Figure 13. Directivities of far-field sound pressure generated by each flow element of unforced shear flow: (a) x = 20–30; (b) x = 30–40; (c) x = 40–50; (d) x = 70–80

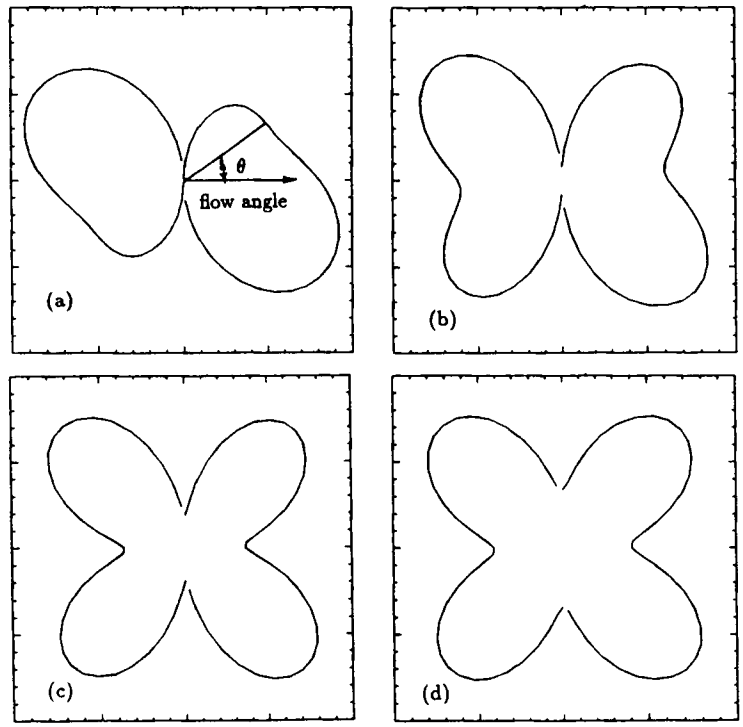

Figure 14. Directivities of far-field sound pressure generated by each flow element of forced shear flow at $St = 0{\cdot}021$: (a) $x = 20$–30; (b) $x = 30$–40; (c) $x = 40$–50; (d) $x = 70$–80

directivity pattern evolves into a lateral quadrupole type, which is shown in Figures 13(c) and 13(d). The sound level maxima are at the angles of $\pm 45°$. The sound level at $-45°$ is slightly higher than at 45°, which indicates that the high-speed side is quieter than the low-speed side. At the flow angle the sound pressure level is minimal. This is a similar situation to the jet noise experiment in which a zone of silence is observed at the flow angle. When forcing is applied at $St = 0{\cdot}021$, the directivity pattern of a single maximum at about the flow angle is distorted faster to become a double-maximum type. This is shown in Figure 14.

Table I lists the maxima of p'_{rms} contributed by each fluid element and their angles for unforced and forced flows. The value of p'_{rms} is modified to be the RMS of $\int [\partial^2 \rho u_r^2 / \partial t^2]^* \, dV$ in equation (12). The number N represents the sound contribution from the flow element $10(N-1) \leqslant x \leqslant 10N$. The increment in θ is 5° and no interpolation is made to yield maximum values and angles. The sound pressure is the single-maximum type for $x \leqslant 30$ and the double-maximum type for $x \geqslant 30$ in all three cases. The far-field p'_{rms} from the flow with low-frequency excitation is greater than that from the unforced flow, while the flow excited by high frequency is the quietest. However, for $x \geqslant 60$ the situation is reversed, so that the high-frequency flow is the loudest, the unforced flow is medium and the low-frequency flow is the quietest. The single-maximum type of directivity pattern is caused by fluid elements where flow fluctuation is at an initial development stage and small. The double-maximum type results from flow with intensified flow fluctuation.

Table I. Local maximum values of p'_{rms} and angles. A contribution is made by each flow element N

	Unforced		$St = 0{\cdot}021$		$St = 0{\cdot}0086$	
N	Angle (deg)	p'_{rms}	Angle (deg)	p'_{rms}	Angle (deg)	p'_{rms}
1	−10	0·104	−10	0·108	−10	0·093
2	−5	0·092	−10	0·095	−10	0·085
3	−10	0·094	−30	0·111	−10	0·084
4	−35	0·126	−40	0·207	−30	0·104
	40	0·099	45	0·181	35	0·091
5	−40	0·289	−45	0·503	−40	0·245
	45	0·266	45	0·481	45	0·221
6	−45	0·543	−45	0·601	−45	0·513
	45	0·520	45	0·532	45	0·482
7	−45	0·689	−45	0·648	−45	0·721
	45	0·660	40	0·607	45	0·680
8	−45	0·718	−45	0·455	−45	0·823
	45	0·696	45	0·443	45	0·789
9	−45	0·855	−45	0·630	−45	0·965
	45	0·822	45	0·647	45	0·942
10	−45	0·910	−45	0·612	−45	1·127
	45	0·897	45	0·621	45	1·086
11	−45	0·877	−40	0·666	−45	1·199
	45	0·851	45	0·644	45	1·155
12	−45	0·963	−40	0·880	−45	1·260
	45	0·936	45	0·829	45	1·226
13	−45	1·118	−45	1·087	−45	1·290
	45	1·066	45	1·014	45	1·230

CONCLUSIONS AND SUGGESTION

The fourth-order Pade compact scheme employed in this work presents flow solutions which exhibit important flow phenomena and agree very well with published experimental theoretical results. The present shear flow solution, when used as a source in the acoustic analogy, successfully renders a typical directivity pattern similar to that caused by a point quadrupole source. The acoustic analogy is a useful method to predict far-field pressure. However, because it uses a known solution with a series of assumptions, some important effects, including refraction, are omitted. If the wave phenomenon is separable from the fluid dynamics, it is suggested that the wave equation be solved numberically to take into account all the physical effects. Let us imagine that away from the flow area there is a region where flow fluctuation is negligible so that a pure acoustic field assumption is valid. In this case the flow and acoustic regions can be separated and the flow equations and wave equation are solved side by side in their respective regions. Pressure information is transferred from the flow region to the acoustic region through the boundary joining the two regions.

REFERENCES

1. M. J. Lighthill, 'On sound generated aerodynamically I. General theory', *Proc. R. Soc. A*, **211**, 564–587 (1952).
2. P. Freymuth, 'On transition in a separated laminar boundary layer', *J. Fluid Mech.*, **25**, 683–704 (1966).

3. G. L. Brown and A. Roshko, 'On density effects and large structure in turbulent mixing layers', *J. Fluid Mech.*, **64,** 775–816 (1974).
4. C. D. Winant and F. K. Browand, 'Vortex pairing mechanism of turbulent mixing-layer growth at moderate Reynolds number', *J. Fluid Mech.*, **63,** 237–255 (1974).
5. S. K. Lele, 'Direct numerical simulation of compressible free shear flow', *AIAA Paper 89-0374*, 1989.
6. S. K. Lele, 'Compact finite difference schemes with spectral like resolution', *J. Comput. Phys.*, **103,** 16–42 (1992).
7. S. T. Yu, Y.-L. P. Tsai and K. C. Hsieh, 'Runge–Kutta methods combined with compact difference schemes for the unsteady Euler equations', *AIAA Paper 92-3210*, 1992.
8. C. K. W. Tam and J. C. Webb, 'Dispersion-relation-preserving finite difference schemes for computational acoustics', *J. Comput. Phys.*, **107**, 262–281 (1993).
9. W. Y. Soh, 'Numerical simulation of free shear flows—towards a predictive computational aeroacoustics capability', *NASA CR 191015*, 1993.
10. A. Jameson, W. Schmidt and E. Turkel, 'Numerical solution of the Euler equations by finite volume methods using Runge–Kutta time stepping schemes', *AIAA Paper 81-1259*, 1981.
11. G. W. Hedstrom, 'Nonreflecting boundary conditions for nonlinear hyperbolic systems', *J. Comput. Phys.*, **30,** 222–237 (1979).
12. K. W. Thompson, 'Time dependent boundary conditions for hyperbolic systems', *J. Comput. Phys.*, **68,** 1–24 (1987).
13. D. Papamoschou and A. Roshko, 'Observations of supersonic free shear layers', *AIAA Paper 86-0162*, 1986.
14. A. Michalke, 'On spatially growing disturbances in an inviscid shear layer', *J. Fluid Mech.*, **23,** 521–544 (1965).
15. P. A. Monkewitz and P. Huerre, 'Influence of the velocity ratio on the spatial instability of mixing layers', *Phys. Fluids*, **25,** 1137–1143 (1982).
16. F. K. Browand, 'An experimental investigation of the instability of an incompressible, separated shear layer', *J. Fluid Mech.*, **26,** 281–307 (1966).
17. C.-M. Ho and L.-S. Huang, 'Subharmonics and vortex merging in mixing layers', *J. Fluid Mech.*, **119,** 443–473 (1982).
18. H. V. Fuchs and A. Michalke, 'Introduction to aerodynamic noise theory', in D. Küchemann (ed.), *Progress in Aerospace Sciences*, Vol. 14, Pergamon, New York, 1973.